Jarno Simola

Millimeter Wave Propagation Measurements and Modeling in Hospital Environments

Faculty of Electronics, Communications and Automation

Thesis submitted for examination for the degree of Master of Science in Technology.
Espoo 28.5.2010

Thesis supervisor:

Prof. Pertti Vainikainen

Thesis instructor:

M.Sc Mikko Kyrö

Aalto University
School of Science
and Technology

AALTO UNIVERSITY
SCHOOL OF SCIENCE AND TECHNOLOGY

ABSTRACT OF THE
MASTER'S THESIS

Author: Jarno Simola

Title: Millimeter Wave Propagation Measurements and Modeling in Hospital Environments

Date: 28.5.2010 Language: English Number of pages: 47

Faculty of Electronics, Communications and Automation
Department of Radio Science and Technology
Professorship: Radio Engineering Code: S-26

Supervisor: Prof. Pertti Vainikainen
Instructor: M.Sc Mikko Kyrö

Applications of wireless technologies in medical treatments have been considered for realizing portable medical equipment and remote monitoring. The 60 GHz band can theoretically offer very high data rates for such applications, but the propagation characteristics of hospital environments have not been studied. Based on preliminary measurements in a shielded room, the propagation characteristics can be expected to be different compared to regular indoor environments.

As a part of a feasibility study of 60 GHz radio systems, propagation channel measurements were performed in two different hospital environments, an angiography room and an ultrasonic inspection room. In this work, path loss and delay domain analysis were made based on the measurement data. Obtained power delay profiles were used to develop delay domain channel models.

The path loss of both hospital environments was found to be similar to common indoor environments. However, the delay domain characteristics of the two rooms turned out to be quite different from each other. Based on this, different models were developed for the environments.

Keywords: Propagation, 60 GHz, channel model, path loss, power delay profile

AALTO-YLIOPISTO DIPLOMITYÖN
TEKNILLINEN KORKEAKOULU TIIVISTELMÄ

Tekijä: Jarno Simola

Työn nimi: Millimetriaaltojen etenemismittaukset ja -mallinnus sairaalaympäristöissä

Päivämäärä: 28.5.2010 Kieli: Englanti Sivumäärä: 47

Elektroniikan, tietoliikenteen ja automaation tiedekunta
Radiotieteen ja -tekniikan laitos
Professuuri: Radiotekniikka Koodi: S-26

Valvoja: Prof. Pertti Vainikainen
Ohjaaja: DI Mikko Kyrö

Langaton tiedonsiirto voi olla hyödyksi monissa lääketieteellisissä sovelluksissa, kuten kannettavissa hoitolaitteissa ja lääkärinhoidon etävalvonnassa. 60 GHz:n taajuusalue tarjoaa teoriassa erittäin nopeaa tiedonsiirtoa kyseisiin sovelluksiin, mutta tiedonsiirtokanavan ominaisuuksia ei ole toistaiseksi tutkittu sairaalaympäristössä. Häiriösuojatussa huoneessa tehtyjen mittausten perusteella näiden ominaisuuksien voidaan olettaa poikkeavan tavallisista sisätiloista.

Osana 60 GHz:n tiedonsiirtojärjestelmien soveltuvuustutkimusta suoritettiin kanavamittauksia kahdessa erilaisessa sairaalaympäristössä, angiografiahuoneessa ja ultraäänitutkimushuoneessa. Mittaustulosten perusteella analysoitiin ympäristöjen etenemisvaimennusta ja viivealueominaisuuksia.

Etenemisvaimennuksen todettiin olevan molemmissa huoneissa hyvin lähellä tavallisten sisätilojen arvoja. Viivealueessa huoneiden siirtokanavat olivat kuitenkin hyvin erilaiset. Angiografiahuoneessa monitie-eteneminen oli voimakkaampaa ja tehoviiveprofiilin muoto erilainen. Tämän vuoksi molemmille ympäristöille kehitettiin oma kanavamalli.

Avainsanat: Radioaaltojen eteneminen, 60 GHz, kanavamalli, etenemisvaimennus, tehoviiveprofiili

Preface

I would like to thank my instructor, Mikko Kyrö and my supervisor, Pertti Vainikainen for all the helpful advice. Thanks to my unofficial supervisor, Katsuyuki Haneda for all of his help and for getting me involved in this project. Thanks to the Radio Laboratory in general for giving me the opportunity to work there for the past year. Also thanks to my family for all the support and understanding during the work.

Otaniemi, 27.5.2010

Jarno Simola

Contents

List of Symbols and Abbreviations

Symbols

ε	permittivity
η	wave impedance
θ	elevation angle
λ	wavelength
μ	permeability
τ	delay
$\bar{\tau}$	mean excess delay
τ_{RMS}	RMS delay spread

d	distance
f	frequency
G	antenna gain
h	channel impulse response
H	transfer function
n	path loss exponent
P	power
PL	path loss
R	reflection coefficient
T	transmission coefficient
w	Gaussian window function
$x(t)$	channel input signal
$y(t)$	channel output signal

Abbreviations

LOS	line-of-sight
NLOS	non-line-of-sight
PDP	Power Delay Profile
RMS	Root Mean Square
Rx	Receiver
Tx	Transmitter
VNA	vector network analyser
WPAN	wireless personal-area network

1 Introduction

The 60 GHz band has some specific features that distinguish it from conventional, lower frequency communication channels. A 7 GHz licence-free spectral space has been allocated in most parts of the world for wireless local communications in the band from 57 to 64 GHz. Due to the short wavelength, antennas can be made very small, and antenna arrays with high directivity can be fitted into small space. Free space path loss is very high compared to lower frequencies due to oxygen absorption, so long-range transmissions are not possible. This higher path loss can be compensated for by using antennas with more directivity, but, when such antennas are used, obstructing the line of sight or misalignment can cause a significant drop of received power. This is because at 60 GHz the diffraction of waves is weak. However, the positive side of high path loss is that it offers the chance for frequency reuse at short distances, for example, in individual rooms inside the same building. Multiple wireless piconets which offer high data-rates can be operated even within the same room using the same frequency.

Wireless communications can offer great benefits for medical applications such as ultrasonic imaging in hospital rooms. When used during surgery, for example, applications like this are very sensitive to latency and reliability issues. Hence, they require real-time video transmission, that can not be compressed. This is why data rates have to be very high, 1 Gbps or even more. The 60 GHz frequency band can offer such data transmission rates. However, certain characteristics of the band, such as quick attenuation against increasing antenna separation and rich multipath components can deteriorate system performance compared to other wireless systems. Therefore it is essential to study the characteristics of 60 GHz propagation channels in hospital environments that may differ from normal indoor environments. Despite plenty of studies on the 60 GHz band in various other indoor environments, there are no measurement results from hospital environments.

The goal of this work was to study the propagation channel characteristics of actual hospital environments for 60 GHz radio. Measurement campaigns were performed by Katsuyuki Haneda and Mikko Kyrö in two different hospital locations, where the measurement scenarios simulate potential medical applications for wireless transmissions. Based on the measurement data, channel characteristics such as path loss

and delay domain properties can be extracted. These characteristics are needed to create channel models, which can be used to easily simulate the behaviour of the propagation channel in hospital environments.

A measurement campaign was performed in a shielded room as a part of the same project as this work. The shielded room environment was assumed to be similar to a hospital surgery room in that the walls are shielded with metal. However, the shielded room was smaller and contained less objects than an actual surgery room. The measurement scenarios were intended to simulate surgeries where the surgeon uses an instrument which has a wireless connection to a display near the surgery table. The measurement is described in detail in [15].

First, an introduction to the theory behind radio wave propagation is given, describing the channel characteristics studied in this work. Previous works on channel measurement and modeling are also briefly reviewed. Next, the channel measurements performed are detailed, covering the measurement system, settings and methods, along with the environments in which the measurements were performed. Finally, measurement data processing methods are explained and the results are reviewed.

2 Basics of Radio Wave Propagation

There are many different types of interactions between electromagnetic waves, the antennas which transmit and receive them, and the environments through which they propagate. All of these effects must be considered in order to understand and analyse the performance of wireless communication systems.

2.1 Indoor Propagation

The indoor radio channel differs from the traditional mobile radio channel in two ways. The distances are much smaller, and the environment can vary much more for a smaller range of Tx-Rx separation. Indoor propagation is strongly influenced by specific features such as the layout of the building, construction materials, and the building type. Still, indoor propagation is governed by the same mechanisms as outdoors: reflection, transmission, diffraction, and scattering.

2.1.1 Reflection and Transmission

Reflection occurs when an electromagnetic wave hits an object which has very large dimensions compared to the wavelength of the wave. Reflections can occur from the surface of the earth and from buildings and walls. The electric field intensity of the reflected and transmitted waves may be related to the incident wave through the Fresnel reflection and transmission coefficients. The reflection coefficient generally depends on the wave polarization, angle of incidence, and the frequency of the propagating wave, and is a function of the material properties, permeability μ and permittivity ε.

In general, planar electromagnetic waves are polarized, meaning they have instantaneous electric field components in orthogonal directions in space. A polarized wave may be mathematically represented as the sum of two spatially orthogonal components, such as vertical and horizontal components. For an arbitrary polarization, the reflected fields from a reflecting surface can be computed using superposition.

When analysing reflection and refraction, it is convenient to work in terms of rays. The situation is shown in Figure 2.1. The plane of incidence is the plane containing the incident, reflected, and transmitted rays. As shown in the figure, part of the

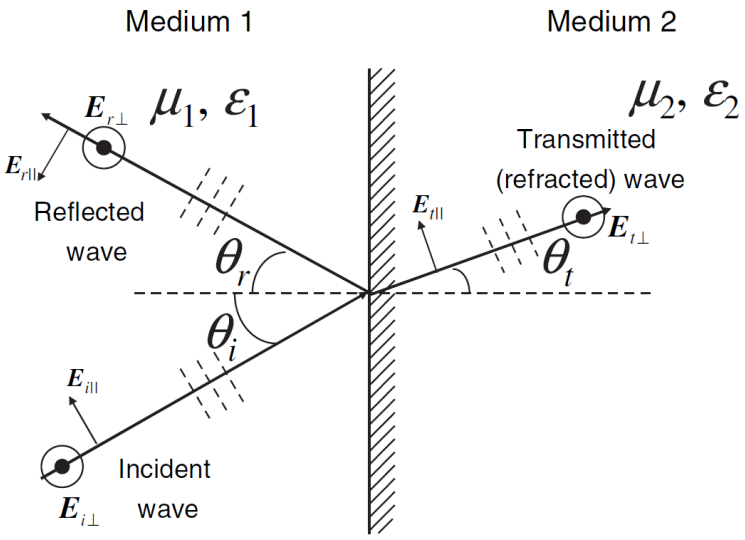

Figure 2.1: Reflection and transmission at the boundary of two materials [1].

energy of the incident wave is reflected back to the first medium at an angle θ_r, and part of the energy is transmitted into the second medium at angle θ_t. The angle of the reflected ray is related to the incidence angle by Snell's law of reflection:

$$\theta_i = \theta_r \tag{2.1}$$

The path of the refracted ray follows Snell's law of refraction:

$$\frac{\sin\theta_i}{\sin\theta_t} = \sqrt{\frac{\varepsilon_2\mu_2}{\varepsilon_1\mu_1}} \tag{2.2}$$

The amplitudes of the reflected and transmitted waves are given relative to the incident wave amplitude by the Fresnel reflection and transmission coefficients. The coefficients are different for cases when the electric field polarization is parallel to the boundary plane, denoted by subscript $\parallel$, and when the electric field is perpendicular to the boundary plane, denoted by $\perp$. The reflection coefficients are denoted by R and the transmission coefficients by T, and are given by

$$R_\parallel = \frac{\eta_2\sin\theta_t - \eta_1\sin\theta_i}{\eta_2\sin\theta_t + \eta_1\sin\theta_i} \quad R_\perp = \frac{\eta_2\sin\theta_i - \eta_1\sin\theta_t}{\eta_2\sin\theta_i + \eta_1\sin\theta_t} \tag{2.3}$$

$$T_\parallel = \frac{2\eta_2\sin\theta_i}{\eta_2\sin\theta_t + \eta_1\sin\theta_i} \quad T_\perp = \frac{2\eta_2\sin\theta_i}{\eta_2\sin\theta_i + \eta_1\sin\theta_t} \tag{2.4}$$

where η_i is the wave impedance of medium i, and is given by $\sqrt{\mu_i/\varepsilon_i}$ [2].

2.1.2 Diffraction

Diffraction occurs when the propagation path between the transmitter and receiver is obstructed by a surface that has a sharp edge. The obstructing surface causes waves to bend around the obstacle, even if there is no line-of-sight path between transmitter and receiver. Diffraction depends on the geometry of the object, as well as the polarization of the incident wave at the point of diffraction.

The phenomenon of diffraction can be understood by using Huygens' principle, which states that each element of a wave front can be considered as a point source for the production of secondary wavelets, and that these wavelets produce a new wave front in the direction of propagation. Diffraction is caused by the propagation of secondary wavelets into areas shadowed by the obstacle [2].

2.1.3 Scattering

Scattering is a process where a wave is forced to deviate from a straight path by one or more localized non-uniformities in the medium through which it passes. This also includes deviation of reflected radiation from the angle predicted by the law of reflection. Reflections that undergo scattering are often called diffuse reflections, while reflections following the Snell's law are called specular reflections. Scattering causes the energy of a radio wave to spread out in many directions. The wave is also depolarized. Scattered waves are produced by rough surfaces, small objects or other irregularities in the propagation path, when the number of these irregularities is large.

The degree of scattering depends on the angle of incidence and the roughness of the surface in comparison to the wavelength. Surface roughness is often defined using the Rayleigh criterion:

$$h_c = \frac{\lambda}{8 \cos \theta_i} \tag{2.5}$$

where λ is the wavelength, and θ_i is the incidence angle. A surface is considered smooth, if the maximum height difference between two points on the surface is less than h_c. Otherwise the surface is considered rough [1].

2.2 Multipath Channel Characteristics

The propagation channel is the part of a communication link between the transmitter and receiver antennas. Millimeter wave indoor radio channel, which is considered in this work, is essentially a multipath channel. If a single pulse is transmitted over a multipath channel then the received signal will appear as a pulse train, with each pulse in the train corresponding to a line-of-sight component, a distinct multipath component from a distinct scatterer and diffuse multipaths from a group of scatterers. The time delay spread of a multipath channel can result in significant distortion of the received signal. Multipath channel parameters such as path loss, delay spread and angle spread describe the statistical properties of the channel.

2.2.1 Path Loss

Path loss is the average of the ratio of the transmitted power to the received power between two antennas, usually expressed in decibels. It includes all kinds of losses associated with interactions between the propagating wave and any objects between the transmitting and receiving antennas. One of the main goals of propagation modelling is to predict path loss as accurately as possible.

The path loss exponent, n is a measure of decay in signal power with distance, d, according to $1/d^n$. Path loss has been shown by many researchers to obey the distance power law, given in decibels as

$$PL(d) = PL(d_0) + 10n\log(d/d_0) \tag{2.6}$$

where d_0 is the reference distance which is determined from measurements close to the transmitter, $PL(d_0)$ is the average measured energy at the reference distance [2].

$PL(d_0)$ depends mainly on the frequency. At 60 GHz path loss is several orders greater than at lower frequencies that are commonly used in wireless communications. Figure 2.2 shows theoretical free-space path loss for 2.5, 5 and 60 GHz.

2.2.2 Fading

In a real propagation environment, path loss is not constant for a given Tx-Rx distance. Objects along a propagation path at a given distance will be different for

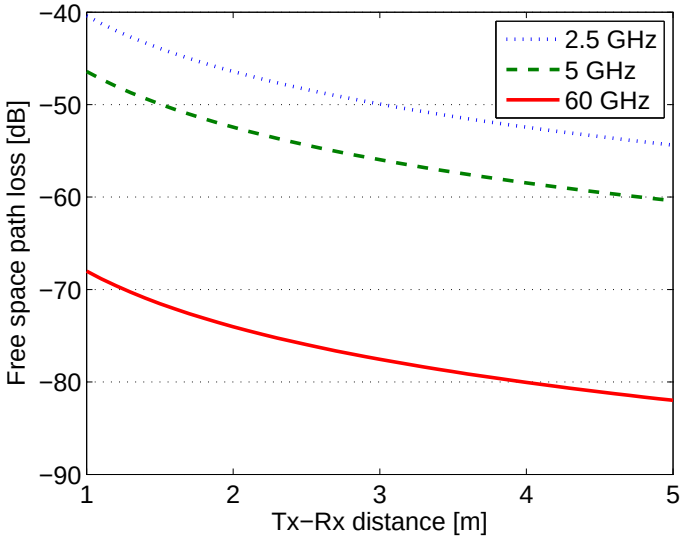

Figure 2.2: Free space path loss against distance for frequencies commonly used in wireless communications. In free space the path loss exponent $n = 2$.

every path, causing variation with respect to the value given by simple path loss models. Some paths will suffer increased loss, while others will be less obstructed and have an increased signal strength. This phenomenon is called shadowing or slow fading.

The effects of shadowing can be included in the path loss model in Equation (2.6) by expanding it to

$$PL(d) = PL(d_0) + 10n \log(d/d_0) + X_\sigma \tag{2.7}$$

where X_σ is a zero mean Gaussian-distributed random variable in dB with standard deviation equal to σ (also in dB) [2].

Even after path loss and shadowing have been predicted for particular locations there is still significant variation in the received signal when an antenna is moved over relatively small distances. The reason for this is that the received signal is a sum of many contributions coming from different directions. Since the phases are random, the sum amplitude varies in a wide range, as much as 30 to 40 dB. This phenomenon is called fast fading and the signal variation is so rapid that it can only be usefully predicted by statistical means.

2.2.3 Impulse Response

Impulse response is a wideband channel characteristic that can be used to derive the information necessary to simulate or analyse any type of radio transmission through the channel. This is because a mobile radio channel may be modeled as a linear system with a time-variant finite impulse response [2]. For a given time t, let $x(t)$ represent the input signal. Then the received signal $y(t)$ can be expressed as a convolution of $x(t)$ with the impulse response $h(t, \tau)$

$$y(t) = x(t) \otimes h(t, \tau) = \int_{-\infty}^{\infty} h(t, \tau) x(t - \tau) d\tau \tag{2.8}$$

where τ is the delay variable.

It is useful to discretize the multipath delay axis τ of the impulse response into equal time delay segments called excess delay bins, where each bin has a time delay width of $\Delta\tau = \tau_{i+1} - \tau_i$. All multipath signals received within the ith bin are represented by a single multipath component having delay τ_i. $\tau_0 = 0$ is the time delay of the first multipath component to arrive to the receiver, after normalizing the propagation delay between the transmitter and receiver. τ_i is the excess delay of the ith multipath component as compared to the first arriving component [2].

2.2.4 Power Delay Profile

The power delay profile (PDP) gives the intensity of a signal received through a multipath channel as a function of time delay. It is defined as

$$P(\tau) = \frac{E[|h(t, \tau)|^2]}{2}, \tag{2.9}$$

where E stands for the ensemble average [1]. Different multipath components can be detected as peaks in a PDP. The PDP can be used to define the following parameters:

- Total excess delay: the difference between the delay of the first and last arriving bin. The last arriving bin can be defined as the greatest excess delay during which multipath power is at a certain level above the noise floor, or the delay during which power falls to X dB below the maximum.

- Mean excess delay : the first moment of the power delay profile, corresponding to the mean value of the PDP. It is defined as

$$\bar{\tau} = \frac{\sum_i P(\tau_i)\tau_i}{\sum_i P(\tau_i)} \tag{2.10}$$

- RMS delay spread: the second moment, or variance, of the profile. This takes into account the relative powers of the bins as well as their delays, making it a better indicator of system performance than the other parameters. It has been shown that under some circumstances, the error probability due to delay dispersion is proportional to the RMS delay only, however, this does not apply to all cases. The RMS delay spread is defined as

$$\tau_{\mathrm{RMS}} = \sqrt{\frac{\sum_i P(\tau_i)\tau_i^2}{\sum_i P(\tau_i)} - (\bar{\tau})^2} \tag{2.11}$$

2.3 Channel Models

Channel models are used to predict the behaviour of radio channels in specific environments without having to measure them. For example, in testing different antennas, it is not realistic to measure every prototype in real environments. Instead, channel models can be used to simulate the channels for the testing of the antenna prototypes. Therefore, channel models should be able to predict, for example, the characteristics described in Chapter 2.2.

There are channel models for different environments, both indoor and outdoor. Indoor channel models can be divided based on the type of building, such as residential, industrial and office environments, or based on the scale of the propagation channel, for example, within a room, within a floor or between floors.

2.3.1 Types of Channel Models

There are three kinds of models for radio wave propagation

- Empirical (or stochastic) models are based on measurement data. They are described with only a few parameters using statistical properties. This has the advantage of taking into account all propagation factors, both known and unknown [1].

- Deterministic models are site-specific. They estimate radio wave propagation analytically. They require huge amounts of accurate geometry information about the location and very high computational effort. Deterministic modeling methods include the finite difference time domain (FDTD) [3], the method of moments (MoM) [4], and ray-tracing (RT) [5].

- Semi-deterministic models are based on empirical models with deterministic aspects, combining both computer simulation results and measurements [6].

2.3.2 Saleh-Valenzuela Model

The Saleh-Valenzuela (SV) model is the most typical empirical model for indoor environments. It is commonly used to describe indoor propagation channel impulse responses. The basic assumption with this model is that multipath components (MPCs) arrive to the receiver in concentrated groups. These concentrated groups of MPCs, also known as clusters, are formed by the multiple reflections from the objects in the vicinity of receiver and transmitter. The clusters, as well as the MPCs within a cluster, arrive according to Poisson processes with different rates and have inter-arrival times that are exponentially distributed. The MPCs amplitudes are independent Rayleigh random variables, and the corresponding phase angles are independent uniform random variables over. The power decays exponentially for clusters and MPCs within a cluster. A typical power delay profile based on the model is shown in Figure 2.3. The impulse response of the channel is given by

$$h(t) = \sum_{l=1}^{\infty} \sum_{k=1}^{\infty} \beta_{kl} e^{j\theta_{kl}} \delta\left(t - T_l - \tau_{kl}\right), \tag{2.12}$$

where T_l is the arrival time of the lth cluster, τ_{kl} is the arrival time of the kth ray measured from the beginning of the lth cluster, while β_{kl} and θ_{kl} are the gain and phase of the the kth ray of the lth cluster. The mean square values of the gain are given by

$$\overline{\beta_{kl}^2} \equiv \overline{\beta^2(T_l, \tau_{kl})} = \overline{\beta^2(0,0)} e^{-T_l/\Gamma} e^{-\tau_{kl}/\gamma}, \tag{2.13}$$

where $\overline{\beta^2(0,0)}$ is the average power gain of the first ray of the first cluster, and Γ and γ are the cluster and ray power decay constants, respectively. T_l and τ_{kl} are described by the independent inter-arrival exponential probability density functions

$$p(T_l|T_{l-1}) = \Lambda \exp\left[-\Lambda\left(T_l - T_{l-1}\right)\right] \tag{2.14}$$

$$p(\tau_{kl}|\tau_{(k-1)l} = \lambda \exp\left[-\lambda\left(\tau_{kl} - \tau_{(k-1)l}\right)\right] \tag{2.15}$$

where Λ and λ are the cluster and ray arrival rate, respectively [7].

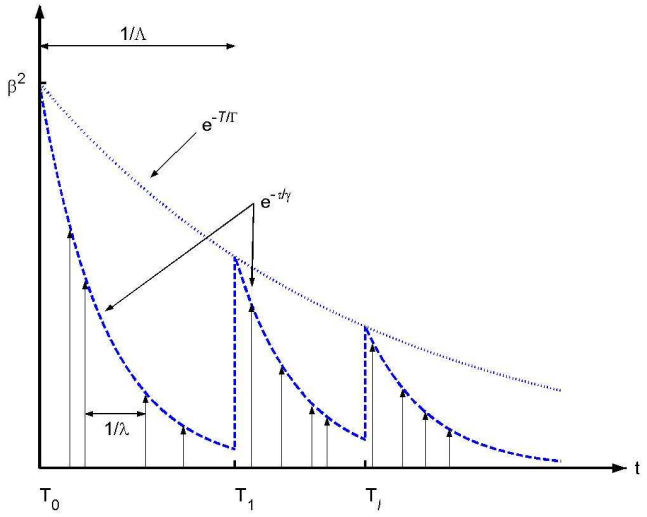

Figure 2.3: A typical power delay profile based on the Saleh-Valenzuela model.

2.4 Review of Channel Measurements

Channel measurements are needed to construct channel models and parameters and to verify theoretical models. The channel measurement data can also be used to evaluate the overall performance of radio systems, e.g. bit rate and reliability.

2.4.1 Measurement Equipment

Channel measurement systems are usually based on either vector network analysers (VNA) or channel sounders. The VNA can be used to measure wider bandwidths and offers flexible frequency control with all the related hardware synchronizations. The drawback of VNA measurement is that the Tx and Rx antennas have to be within cable length. The VNA uses a stepped frequency sweep to measure the channel in the frequency domain, which, especially in wideband measurements, leads to longer measurement times. A channel sounder usually means a measurements system consisting of a transmitter, receiver, and a fast data acquisition unit. So, contrary to a VNA, the transmitter and the receiver rely individually on accurate, synchronized reference oscillators, which allows greater measurement distances. Channel sounders can be used to gather large number of samples quickly and, hence, enable very fast propagation channel measurements.

2.4.2 Channel Measurements in 60 GHz band

Channel measurements at 60 GHz have focused mainly on indoor environments because of its main application, wireless personal-area networks (WPAN). The first 60 GHz channel measurements were reported in the 1990s. For example, [8] reports several narrowband and wideband measurements in both indoor and outdoor environments. The measurement system used for narrowband measurements was based on a spectrum analyzer and the wideband measurements had been done with a VNA.

Since then, a substantial amount of 60 GHz range measurements have been performed, mostly concentrating on the delay domain. [9] describes a wideband channel sounder covering 5 GHz of bandwidth with 0.2 ns channel impulse response resolution and channel measurements from several different rooms (offices, labs and conference rooms). [12] presents a VNA-based MIMO measurement system with a fine time resolution.

[10] presents a measurement campaign and delay domain characterization of corridor and office locations. Path loss values are measured for several different indoor environments, for example, in [14], [16], and [17]. Several measurement campaigns from different indoor environments are also summarized in [13].

3 Channel Measurements

This chapter lists the measurement equipment and methods used in this work, and describes the measurement locations and scenarios in a hospital. Some of the potential wireless applications that motivated this work, are also described. Finally, antenna radiation pattern measurements conducted in an anechoic chamber are reported.

3.1 Measurement Equipment

The measurement system combines a vector network analyser (VNA) with frequency converters as shown in Fig. 3.1. Detailed information about the frequency converters can be found in [11]. The VNA used in this work is an Agilent E8363A which sweeps the intermediate frequency (IF) signal from 5 to 9 GHz with 2 MHz frequency spacing. A signal covering from 61 to 65 GHz is generated at the frequency up converter by mixing the IF signal with a 14 GHz local carrier signal. The same local carrier signal was supplied to the down converter in order to synchronize the transmitter and the receiver and to avoid phase drifts. The phase of the local oscillator was locked to the VNA with a 10 MHz reference signal. Having set the intermediate frequency bandwidth of the VNA to 30 kHz, it was possible to perform acquisition of transfer functions 6.5 times a second. More detailed information about the measurement system can be found in [12]. The measurement settings are listed in Table 3.1. The same settings were used in all measurement campaigns.

Table 3.1: Measurement settings.

RF frequency	61-65 GHz
IF frequency	5-9 GHz
LO frequency	14 GHz
VNA IF bandwidth	30 kHz
VNA output power	7 dBm
Number of frequency steps	2001
Signal generator output power	18 dBm

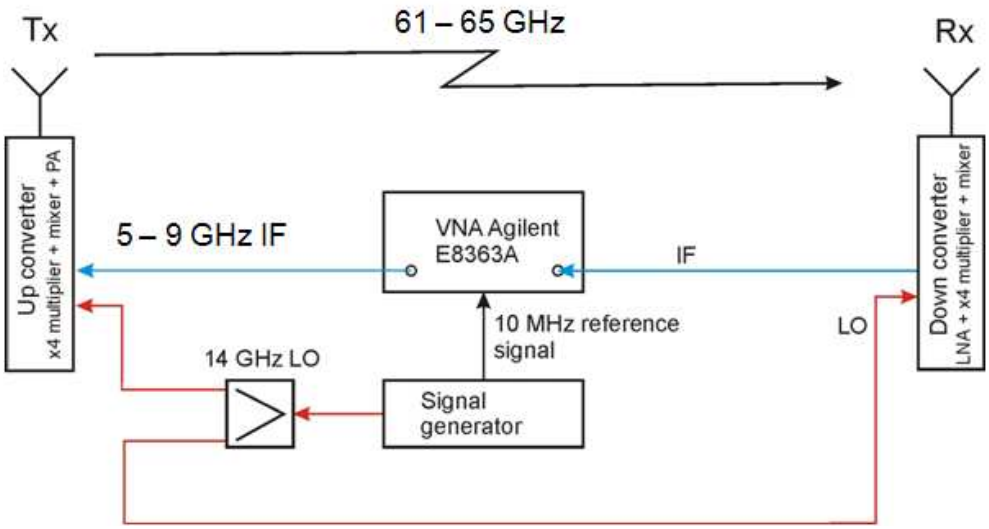

Figure 3.1: Schematic of the measurement system.

(a) **(b)**

Figure 3.2: The antennas used in the measurements, a biconical antenna (a) and an open-ended waveguide (b).

3.2 Back-to-Back Calibration Measurements

To remove the effect of measurement equipment from the measurement results, a back-to-back calibration measurement was performed before every measurement campaign. In a back-to-back measurement the measurement set-up is the same as in actual channel measurements, except for the antennas. In this case the waveguides connected to the up and down converters on the transmitting and receiving sides were connected through a 20 dB attenuator. When the open-ended waveguide was used as an antenna, it was not removed. The back-to-back measurement provides a

transfer function without the antennas and propagation channel. When processing the measured data, the transfer function of the actual measurement is divided by the back-to-back transfer function to remove the effect of measurement equipment from the results in order to obtain the transfer functions of the antennas and the propagation channel.

3.3 Shielded Room Measurements

A propagation measurement was performed by Katsuyuki Haneda and Mikko Kyrö in a shielded room as a preliminary work for the actual hospital measurements. The measurement in a shielded room is meaningful for studying propagation characteristics in medical applications, since real surgery rooms are typically shielded. This measurement was intended to simulate a usage scenario of real-time video streaming for ultrasonic imaging.

The room was shielded with metal walls and had dimensions of 6 m in width, 3.7 m in depth, and 2 m in height as shown in Fig. 3.3. The Tx antenna was mounted on a tripod and placed on 16 different positions around the table where the patient was laying. This table was 0.8 m high and made of a wooden panel on a metallic frame. The Rx antenna, together with the frequency converter, was attached to the arm of a physician and was moved above the patient to emulate several typical movements of the physician performing the ultrasonic imaging. The five scenarios are depicted in Fig 3.4a. In scenarios 1 and 2 the physician rotates the Rx antenna clockwise and counter clockwise as shown in black and red arrows. Scenarios 4 and 5, shown in green and violet arrows, emulate the physician's hand movement during the ultrasonic imaging of a pregnant woman. The physician moves the Rx antenna left-right and back-forth on a semi-spherical surface. The movement of the hand was repeated three times for each scenario. In scenario 3 the Rx antenna was kept static above the abdomen of the patient for about 20 seconds to monitor the influence of the breathing of the patient. These five scenarios were measured for each of the 16 positions of the Tx antenna. The location of the physician and the patient was the same for the entire measurement as shown in Fig. 3.3 [15].

Open-ended waveguides were used as both the Tx and Rx antennas. Azimuthal orientation of the Tx antenna was determined so that its broadside was directed toward

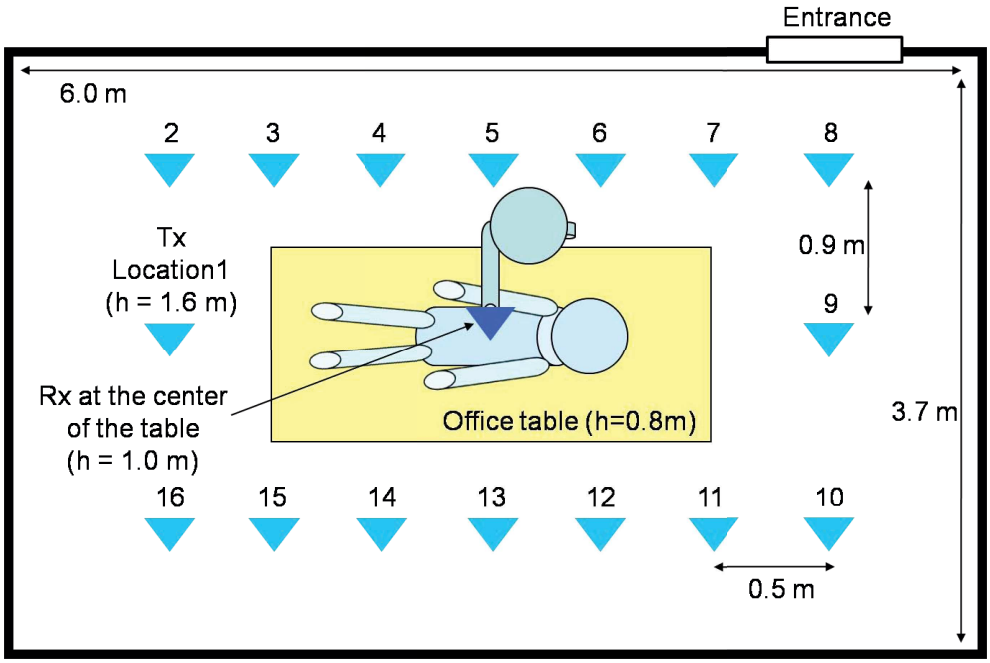

Figure 3.3: The floor plan of the measurement scenario in the shielded room.

the Rx antenna, while there was no adjustment of the broadside on the elevation orientation. The Rx antenna was oriented so that the broadside is pointing toward the ceiling directly above, except for scenarios 4 and 5 where the antenna can point off from that direction due to the semi-spherical movement of the hand [15].

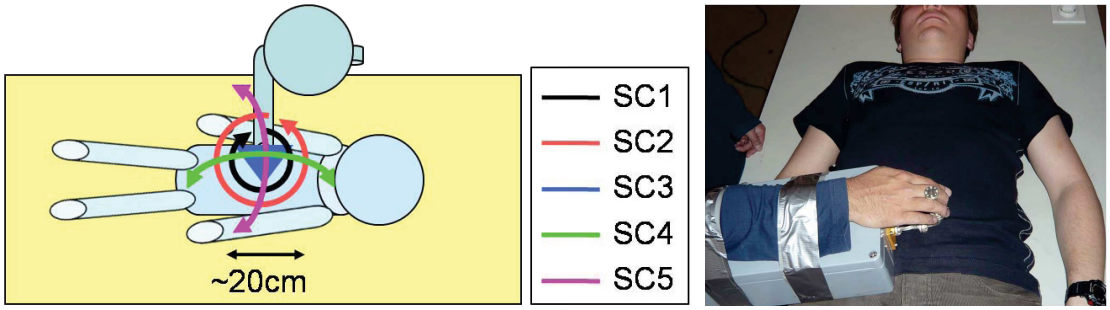

(a) (b)

Figure 3.4: (a) Definition of five hand moving scenarios on the physician side antenna. (b) Settings of the Rx antenna and down-converter on the physician side.

3.4 Hospital Measurements

This measurement campaign was performed by Mikko Kyrö and Katsuyuki Haneda at Yokohama City University Hospital, Japan. The purpose of the measurements was to examine two possible medical applications for wireless video transmission; angiography examination and ultrasonic imaging. In angiography examination, X-ray imaging is used to monitor the location of the head of a catheter inside a human body. In ultrasonic imaging, a physician monitors synthesized images measured by a hand-held probe. The use of wireless connection between the device and the display provides flexibility in display locations and postures of the patient under inspection, thus leading to efficient operation. The first series of measurements was performed in an angiography room and another series in an ultrasonic inspection room.

3.4.1 Angiography Room Measurements

In the angiography room, the measurement assumes a usage scenario of real-time video streaming from an X-ray device to a movable screen. The screen is hanging from the ceiling and it can be placed anywhere around a surgery bed. For this reason the transmitter (Tx) antenna was moved to 39 different positions around the surgery bed. The receiver (Rx) antenna was placed at two different positions since there were two X-ray machines taking images for horizontal and vertical cross sections for body and head of patient, respectively. Figure 3.5 shows a photograph of the measurement environment.

Three different measurement scenarios were examined in the angiography room measurements. The first scenario was a static measurement which was used as a reference for the other scenarios. A static measurement means that neither of the antennas is moved and the whole measurement environment is kept as static as possible. The purpose of the second scenario was to study the effect of the human body shadowing the line of sight. This was done by having people move between Tx and Rx during the measurement, so that the line-of-sight link is often shadowed. The third scenario was a static measurement with varying Tx antenna height within the range of 20 cm. These results were used to derive path loss values and power delay profiles. The antenna height is varied for spatial averaging, which is used to remove the effect of fast fading from the results.

Figure 3.5: Photo of the angiography room.

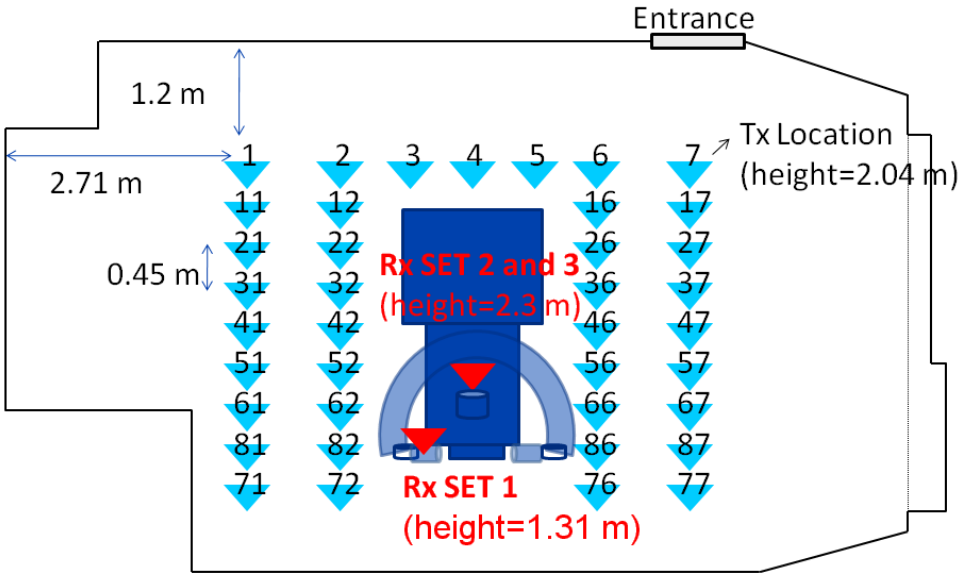

Figure 3.6: The floor plan of the angiography room including Tx and Rx antenna locations.

In the first measurement set the Rx was placed at location 1 on top of the horizontal X-ray device, and all scenarios were measured. In this set a biconical antenna that is omnidirectional in the horizontal plane was used as a Tx antenna and a unidirectional open-ended waveguide was used as an Rx antenna. In measurement sets 2 and 3, only the third measurement scenario was considered, because both Tx and Rx were located so high, that human body shadowing could be ignored. In these

sets biconical antennas were used at both ends of the link. The Rx antenna was placed on top of the vertical X-ray device. In set 3 the horizontal X-ray device was also placed over the bed, causing some Tx locations to be shadowed.

3.4.2 Ultrasonic Inspection Room Measurements

In the ultrasonic inspection room measurements, different usage scenarios of real-time video streaming for ultrasonic imaging were investigated. The room was equipped with four ultrasonic imaging devices and beds. These beds were separated with curtains. In the measurements the Tx antenna was placed on each bed and the Rx antenna was moved to different locations around the bed. The measurements were performed with two Rx antenna heights (1.58 m and 2.29 m) corresponding to the possible heights of the antennas for the display of the ultrasonic imaging machine. The height of the Tx antenna on the beds was 0.75 m, assuming an antenna attached to a probe for a patient lying on the bed. Figure 3.7 shows a photograph of the measurement setting with the Rx antenna at 2.29 m. A floor plan of the environment is shown in Figure 3.8.

Figure 3.7: Photo from the ultrasonic inspection room.

The measurements in the ultrasonic inspection room consisted of three different

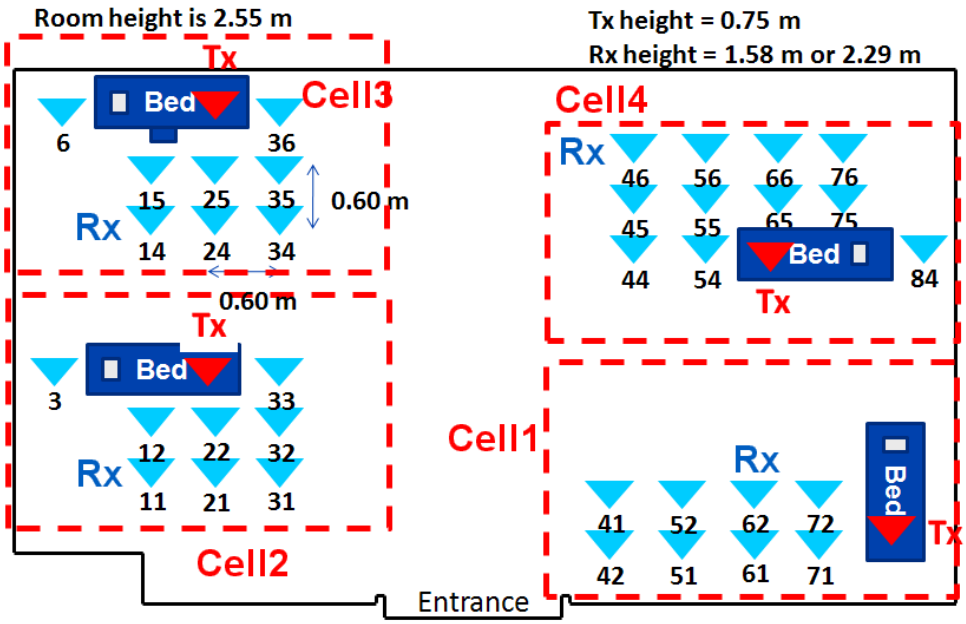

Figure 3.8: Floor plan of the ultrasonic inspection room.

measurements. The first measurement was a co-polarization measurement to investigate dominant propagation mechanisms of the channels. Both Tx and Rx antenna were set to radiate vertical polarization. The second measurement was intended to examine the cross-polarization ratio of the channel by rotating the Rx antenna to radiate horizontal waves. In the third measurement interference between neighbouring links of ultrasonic imaging equipment operated at the same frequency band was investigated. In this measurement a piconet is formed for each ultrasonic imaging equipment, and therefore, the interference comes from piconets operated at neighbouring beds.

3.5 Radiation Pattern Measurements

To derive the path loss of a propagation channel from measurement data, one has to subtract the effect of the measurement equipment, including antennas. This requires knowledge of the radiation patterns of the antennas. To this end, antenna gain measurements were performed in an anechoic chamber. These measurements focused on radiation patterns in the elevation plane. Azimuth angles were not measured because the biconical antenna is omnidirectional, i.e., it can be assumed to radiate uniformly in the azimuth plane. For the open-ended waveguide, only the

elevation pattern was measured and simulated patterns were used for the azimuth. The patterns were used in compensating for the antenna radiation patterns, which is described in Chapter 4.

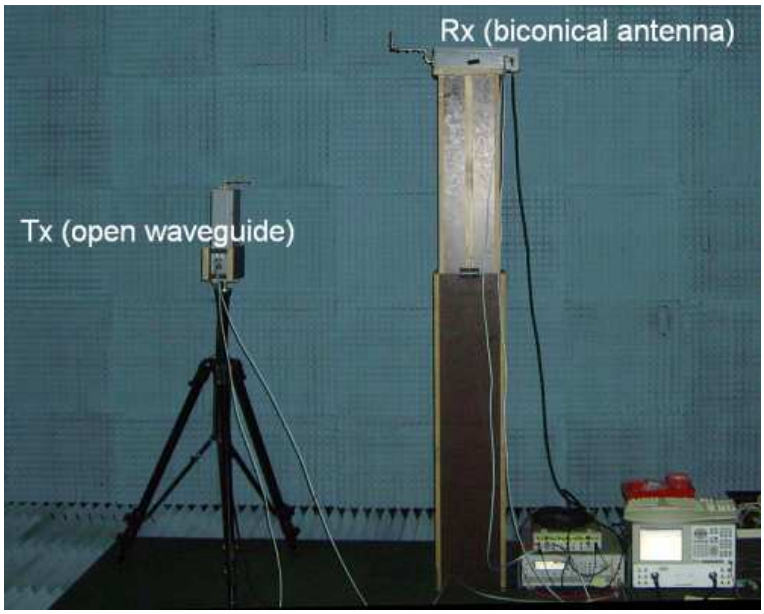

Figure 3.9: The antenna radiation pattern measurement set-up.

The measurements were performed with a resolution of 5° for elevation angles from 0 to 65 degrees for the Tx antenna, and 0 to -65 for the Rx, corresponding to the maximum elevation range in the hospital measurements. The azimuth angle was set to 0, i.e., the antennas were facing each other. The Tx antenna was placed on a tripod and the Rx antenna on top of a wooden antenna tower with adjustable height. The horizontal distance of the antennas was kept constant, and different elevation angles were achieved by changing the height of the antennas. These are detailed in table 4.1. Three different antenna combinations were measured:

- Tx biconical antenna, Rx biconical antenna
- Tx biconical antenna, Rx open-ended waveguide
- Tx open-ended waveguide, Rx biconical antenna

These combinations corresponded to all the different antenna combinations used in the hospital measurements. Therefore it was not necessary to obtain radiation patterns for individual antennas. The measurement settings were the same as described

in Table 3.1 except for the signal generator output power, which was 10 dBm in this case, because of shorter Tx-Rx distances.

Table 3.2: Measurement settings.

Vertical Tx-Rx distance	0.6 m
Antenna height difference	0 - 1.29 m
Elevation angle	$-65°$ - $65°$
Number of elevation angles measured	14

4 Data Processing and Results

This chapter describes the data processing methodologies and the corresponding results. Based on these results propagation channel models are developed for different hospital environments.

4.1 Antenna Radiation Patterns

Since the transfer functions measured in an anechoic chamber for antenna radiation pattern contained both antenna gain and propagation loss, it was necessary to post-process the measured data to obtain the antenna gain. The path loss was derived from the measured transfer function by

$$PL_{\text{measured}} = -10\log_{10}\left(\frac{1}{S}\sum_{s=1}^{S}|H(s)|^2\right) \tag{4.1}$$

where $1 \leq s \leq S$ denotes the snapshot index of transfer functions and H is the transfer function.

It was assumed that in an anechoic chamber, with a clear and unobstructed line-of-sight path between the antennas, path loss would follow the free space propagation model. The measured path loss with free space model and antenna gains is given by

$$PL_{\text{measured}} = -10\log_{10}\left[\frac{G\lambda^2}{(4\pi)^2 d^2}\right] \tag{4.2}$$

where $G = G_{\text{t}}G_{\text{r}}$ is a combination of the transmitter and receiver antenna gain, d is the Tx-Rx separation distance in meters, and λ is the wavelength in meters. In wideband measurements, the wavelength corresponding to the center frequency is used. Knowing this, the combined antenna gain (in dB) of the transmitter and the receiver can be calculated from the measured path loss by

$$G = PL_{\text{measured}} + 10\log_{10}\left[\frac{\lambda^2}{(4\pi)^2 d^2}\right]. \tag{4.3}$$

The elevation angle can be calculated by

$$\theta = \arctan\left(\frac{\Delta h}{d_{\text{h}}}\right) \tag{4.4}$$

where Δh is the height difference of the antennas and d_{h} is the horizontal distance between the antennas.

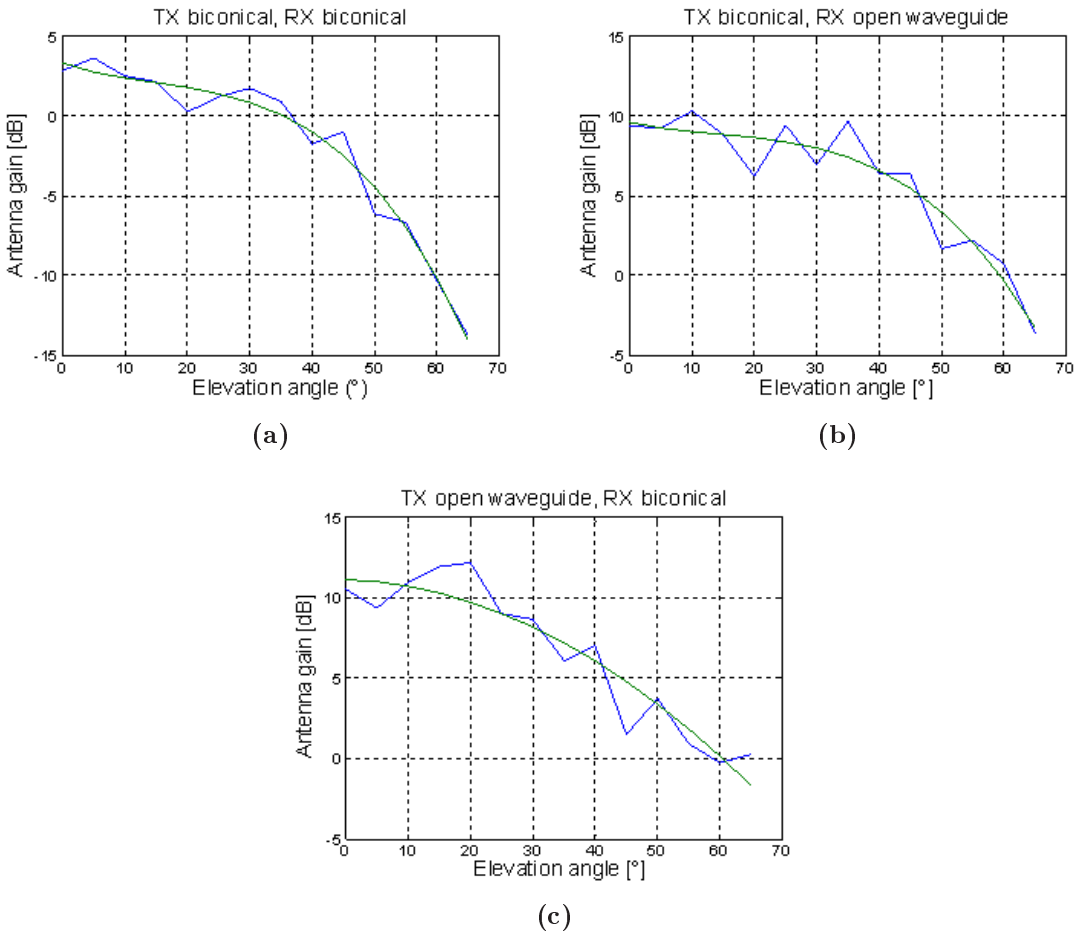

Figure 4.1: Measured antenna elevation gains: (a) both Tx and Rx antenna are biconical, (b) Tx biconical, Rx open-ended waveguide, (c) Tx open-ended waveguide, Rx biconical.

The combined antenna gain was calculated for each measured elevation angle as shown in Figure 4.1. The measured data for each antenna combination was fitted with a polynomial function, which was used to subtract the antenna gain from the hospital measurement results. There was some fluctuation in the results, possibly due to side lobes in the radiation patterns or reflections. However, the fitted functions were consistent between different antenna combinations and compared to simulated radiation patterns at least for smaller elevation angles, so the results were considered sufficient.

4.2 Path Loss Model

Path loss model for the shielded room was derived by Mikko Kyrö at [15], and therefore, this thesis does not cover the result. Only the path loss models in the hospital room measurements are presented here.

4.2.1 Derivation

The path loss of propagation channels was calculated for each Tx-Rx combination by

$$PL_l = -10 \log_{10} \left(\frac{1}{S} \sum_{s=1}^{S} |H_l(s)|^2 \right) - G(\theta_l) \tag{4.5}$$

where $1 \leq s \leq S$ denotes the snapshot index of transfer functions, l is the index of the location of Tx or Rx, depending on which antenna was moved in the particular measurement; H_l is the transfer function for that location; $G(\theta_l)$ is the combined antenna gain corresponding to θ_l which is the elevation angle corresponding to the location, calculated by

$$\theta_l = \arctan \left(\frac{z_l}{\sqrt{x_l^2 + y_l^2}} \right) \tag{4.6}$$

when the Rx antenna location l is in coordinates (x_l, y_l, z_l) compared to the Tx antenna, i.e. Tx is placed at the origin.

4.2.2 Model

The path loss exponent is obtained by performing least squares regression analysis on the logarithmic scatter plot of the path loss against the Tx-Rx distance. The value of $d_0 = 1$ m is used as reference distance in all cases.

Path loss for the angiography room was determined based on measurement set 2, where there were no objects shadowing the link between Tx and Rx. The result is plotted in Figure 4.2 with its best fit expressed by

$$PL(d) = 66.7 + 18.6 \cdot \log_{10}(d). \tag{4.7}$$

The Tx-Rx distance dependency of the path loss in the ultrasonic inspection room is shown in Figure 4.3. This figure combines results for both Rx heights in the

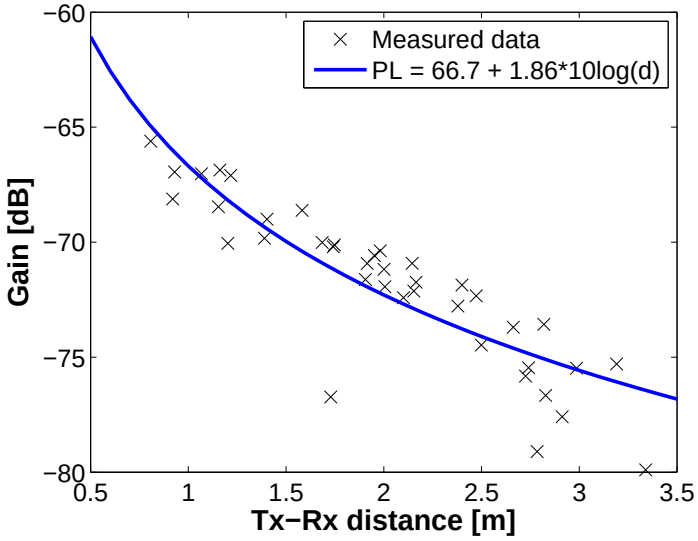

Figure 4.2: Path loss modeling in the angiography room against the Tx-Rx distance.

co-polarization measurements and the interference measurements, where Tx-Rx distances were greater. The results can be best fitted the equation:

$$PL(d) = 67.1 + 22.3 \cdot \log_{10}(d). \tag{4.8}$$

The effect of the antenna gain compensation can be seen by comparing Figure 4.3 with Figure 4.4, which shows the measured path loss values without antenna gain compensation. Without the compensation it would not be possible to get a single path loss model for the ultrasonic inspection room.

These measurement results can be compared to the IEEE P802.15 TG3c channel model [13] which is currently the most extensive channel model for 60 GHz wireless personal area network (WPAN) applications. The TG3c model has the same form that is used in this work, defined by Equation (2.6). According to the model the path loss exponent n varies from 1.2 to 2.0 for LOS environments. The parameter values are detailed in Table 4.1. The path loss exponent and the initial path loss $PL(d_0)$ for the angiography room were approximately the same as for a small furnished room [14]. $PL(d_0)$ for the ultrasonic inspection room was also close to that of the small room and a kiosk environment [16]. The path loss exponent for the ultrasonic inspection room was mostly larger than that of LOS environments in the

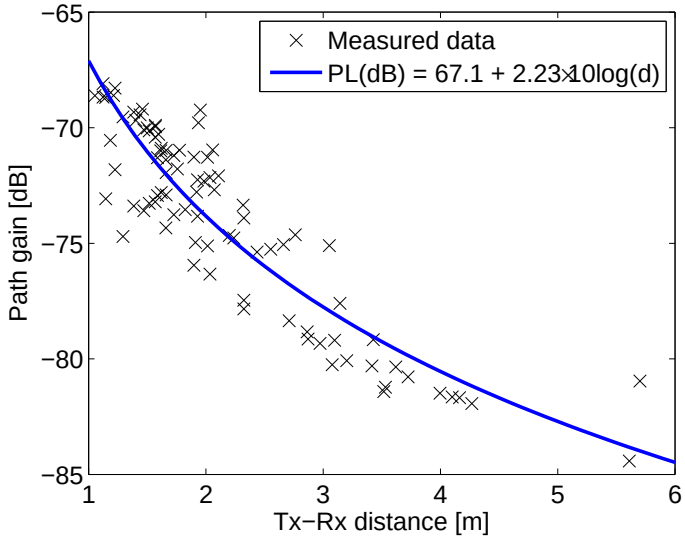

Figure 4.3: Path loss results for the ultrasonic inspection room measurement compared to the Tx-Rx distance.

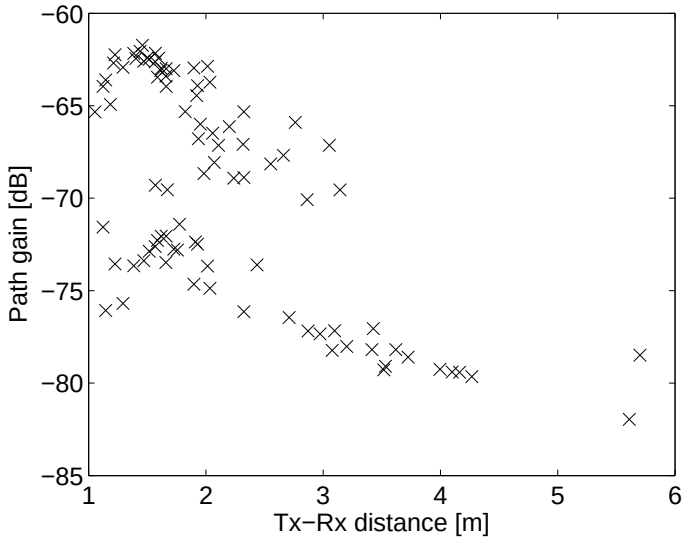

Figure 4.4: Path loss without antenna gain compensation for the ultrasonic inspection room measurement against the Tx-Rx distance.

TG3c channel model, except for the one in an empty shielded room which shows a significantly larger value [15].

Table 4.1: Parameters for the path loss model in the hospital environments and in different LOS scenarios reported in the literature for 60 GHz radio channels.

Environment	n	$PL(d_0)$	Ref.
Angiography room	1.86	66.7	
Ultrasonic inspection room	2.23	67.1	
Small furnished room	1.7	65	[14]
Kiosk	N/A	68	[16]
Shielded room	4.18	73.7	[15]
Residential	1.53	75.1	[17]

4.3 Delay Domain Channel Model

In this section, it is described how the power delay profiles were derived from the measurement data. The PDP's are used to determine suitable delay domain channel models, and then parameters for these models are extracted.

4.3.1 Power Delay Profile

The delay domain characteristics of the propagation channels were examined with power delay profiles. The PDP's were derived from the transfer functions by

$$P(\tau_k) = E\left[\frac{1}{K}\sum_{k=1}^{K} w_k H_k \exp\left(j2\pi \cdot f_k \tau_k\right)\right] \tag{4.9}$$

where f_k is the baseband frequency corresponding to the kth frequency bin, τ_k is the delay time, $1 \leq k \leq K$. The ensemble average E was taken over all measured snapshots in each combination of Tx-Rx locations; w_k denotes a windowing function to reduce side lobe levels. In this analysis, the Gaussian window function

$$w_k = \exp\left[-\frac{1}{2}\left(\alpha\frac{k-1-(K-1)/2}{(K-1)/2}\right)^2\right] \tag{4.10}$$

was used with $\alpha = 2.5$.

It was found that the PDP's for the angiography and ultrasonic inspection rooms were significantly different, as can be seen in Figure 4.5. In the angiography room

the specular components, which appear as peaks or spikes, were more clearly identifiable than in the ultrasonic inspection room. Also, the decay of the power seemed to follow a different shape. Therefore it was necessary to analyse and model the two environments differently. The PDP's of the ultrasonic inspection room were similar to those of the shielded room with few specular components.

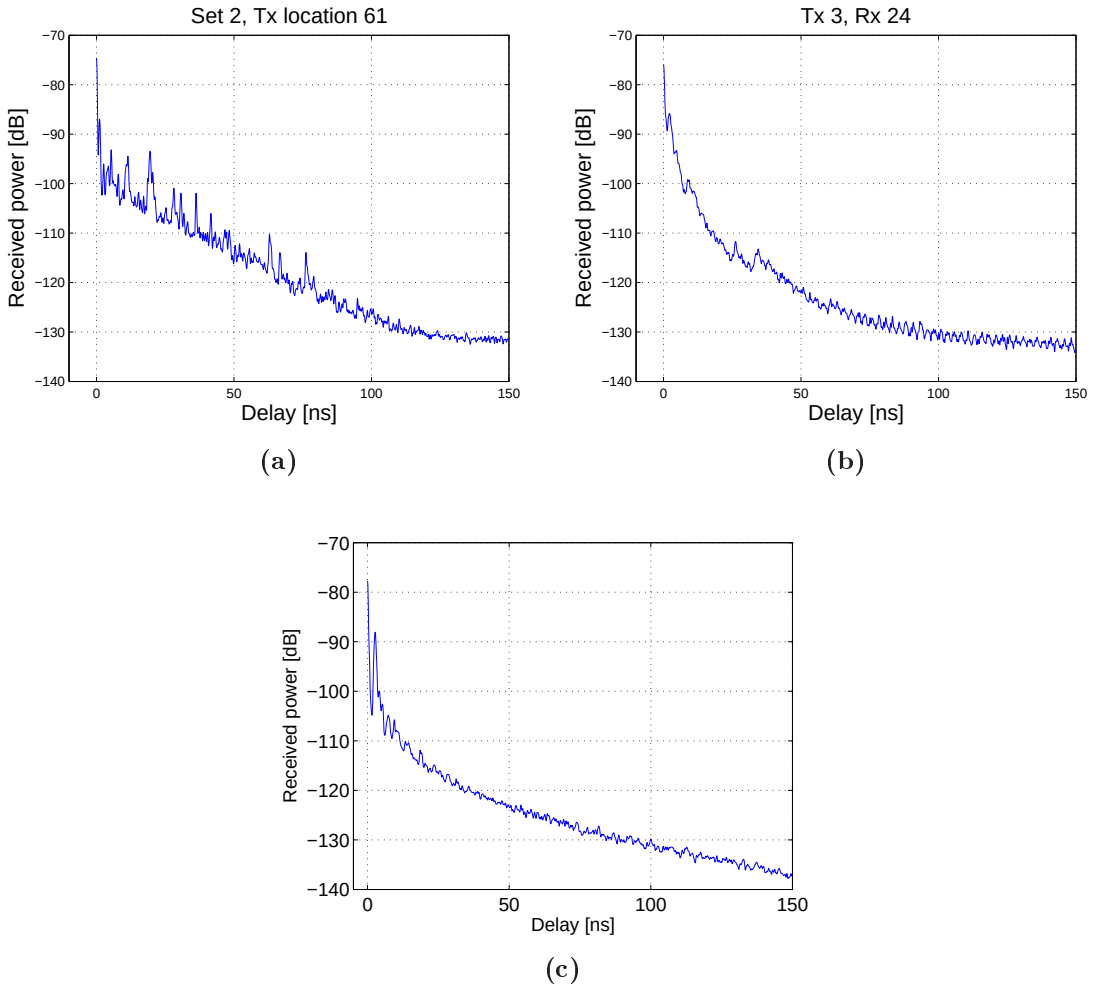

Figure 4.5: Typical power delay profiles for the angiography room (a), the ultrasonic inspection room (b), and the shielded room (c).

4.3.2 Model Description

Mathematical models, that would best express the delay domain behaviour of the propagation channel, were developed for both the angiography room and the ultrasonic inspection room.

Model for the angiography room According to Figure 4.5a, the PDP model for the angiography room should include specular components that appear as narrow peaks and a diffuse component that follows an exponential decay model. So, the PDP is expressed as

$$PDP(\tau) = \sum_{n=1}^{N} P_n \delta(\tau - \tau_n) + P_{0\text{dif}} \exp\left(-\beta\left(\tau - \tau_0\right)\right), \tag{4.11}$$

where N is the number of the specular components, P_n and τ_n the power level and the excess delay of the nth specular component, $P_{0\text{dif}}$ and β the peak power level and the decay constant of the diffuse component and τ_0 is the delay of the first arriving component. Similar decay of the diffuse component has been reported in [18].

Model for the shielded room and the ultrasonic inspection room As Figure 4.5b shows, power delay profiles in the ultrasonic inspection room consist of several identifiable clusters. The cluster starts from a distinguishable peak, followed by a decaying tail of power. It was found that an exponential power decay model, which has been widely observed in channel measurements, e.g. the Saleh-Valenzuela model [7], could not be used to model the PDP's in this environment, since the measured PDP decays much steeper than the exponential decay law. Therefore, it was decided to use a power law model for the curve fitting. Similar decay has also been observed in [19] and [20]. The power law model provides steeper decay and better fit to the measured curves.

In the power law model the power of a cluster n is defined as

$$P_n(\tau) = \begin{cases} 0 & \tau < 0 \\ P_{n0}\left(\tau + \tau_{n0}\right)^{-\alpha_n} & \tau \geq 0 \end{cases} \tag{4.12}$$

where P_{n0}, τ_{n0} and α_n are the initial power value, offset delay and decay constant for the nth cluster, respectively. The power at any given time τ in the PDP can be calculated by

$$PDP(\tau) = \sum_{n=1}^{N} P_n\left(\tau - \lambda_n\right) \tag{4.13}$$

where λ_n is the delay time from which the nth cluster begins.

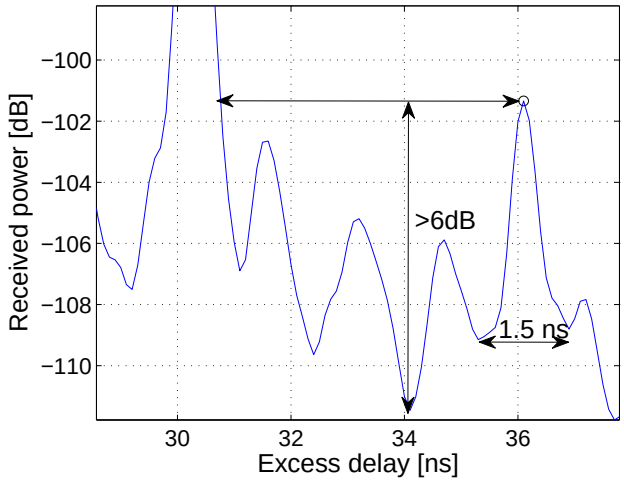

Figure 4.6: An illustration of the peak search method and windowing for fitting diffuse components.

4.3.3 Model Parameter Identification

It was necessary to identify the specular components in the model for the angiography room and the beginning of clusters in the model for the ultrasonic inspection room and the shielded room in order to derive the delay domain model parameters. A peak search algorithm was developed to allow automatic identification of multipath components. The search algorithm first finds all local maxima from the PDP, then, for every individual maximum, traces backwards on the delay until it finds a point where the power is higher than that at the present peak of interest. For that delay interval the algorithm finds the minimum power value and calculates the power difference between the minimum and the peak. This is illustrated in figure 4.6. The peaks that have a power difference of over 6 dB are chosen as the starting points of the clusters. Based on testing, the value of 6 dB seemed to fit well with visual observations.

For the angiography room, the diffuse part of the power seems to follow a straight line on the decibel scale, therefore the decay of the power is modelled as an exponential function of the excess delay. Before the diffuse part can be fitted, the specular components have to be discarded. This was done by taking a 1.5 ns section around every detected peak in the PDP and ignoring it when fitting the data. The parameters of the power law model were found based on least squares fitting for

individual clusters. However, since precise fitting of cluster peaks is more important than its tail, an weighting vector was introduced. A cost function to be minimized was defined as

$$E = ||\mathbf{w} \diamond (\mathbf{P}_{\text{measured}} - \mathbf{P}_{\text{fit}})||^2 \tag{4.14}$$

where $\diamond$ is an operation of element-wise multiplication; $\mathbf{w} = [w_1 \quad 1 \quad 1 \quad \dots \quad 1]^T$ denotes the weighting vector; $\cdot^T$ is a transpose operation. In this work, w_1 was set to 20. Based on extensive testing, it was found that weighting the first delay of clusters provides satisfactory results; $10 < w_1 < 100$ worked best.

These simple criteria provide reasonable results which agree very well with visual inspections. The exemplary PDP shown in Fig. 4.12 has 3 peaks that satisfies $\Delta P > 3$ dB, thereby the cost function in Eq.(4.14) revealed the smallest value.

4.3.4 Results and Discussions

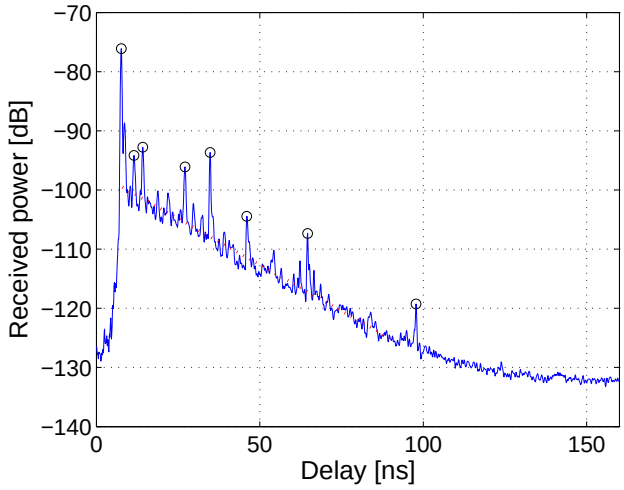

Figure 4.7: A PDP from the angiography room with detected specular components and fitted diffuse.

Angiography Room The model parameters for the angiography room were derived from the PDP's. Figure 4.7 shows an example of a PDP from the room with identified specular components appearing as peaks and diffuse component fitted by a linear red line. Due to the limited time of the thesis, the modeling of the ultrasonic inspection room was left for future work.

The diffuse component parameters, $P_{0\text{dif}}$ and β were found to have some correlation to Tx-Rx distance and LOS power, but this effect was no more than a few decibels over the excess delay range where the power is above noise level. The difference of LOS power and diffuse peak power P_{0dif} against Tx-Rx distance is plotted in Figure 4.8. It is clearly seen that the difference decreases with growing Tx-Rx distance. The diffuse decay constant β also seems to exhibit linear dependency on growing Tx-Rx distance, but the variation of the constant is very little, as shown in Figure 4.9.

The power of the specular components also seemed to depend linearly on the excess delay on the logarithmic scale, despite a lot of variance, as can be seen in Figure 4.10. The figure combines results from all measurement locations, and the power and delay of each specular component was normalized to that of the LOS. The best fit for the linear dependency is expressed by

$$P_{\text{spec}}(\tau) = P_{\text{LOS}} - 13.9 - 0.34(\tau). \tag{4.15}$$

The number of detected specular components varied between 7 and 14. The number did not seem to correlate with either Tx-Rx distance or other parameters. The distribution of the number of components is shown in Figure 4.11. Based on this and the distribution of the components in excess delay, reflections from both objects and walls are strong in the angiography room.

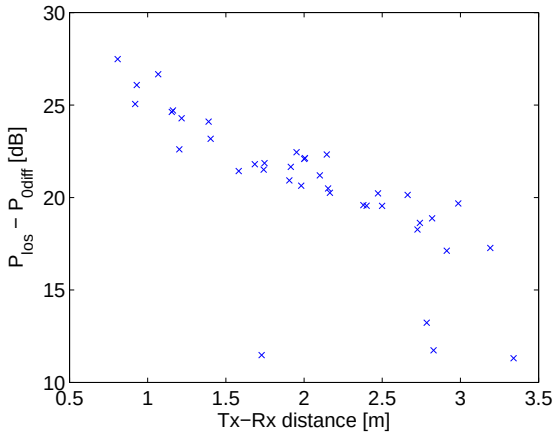

Figure 4.8: The difference of LOS power and diffuse offset power against Tx-Rx distance in the angiography room.

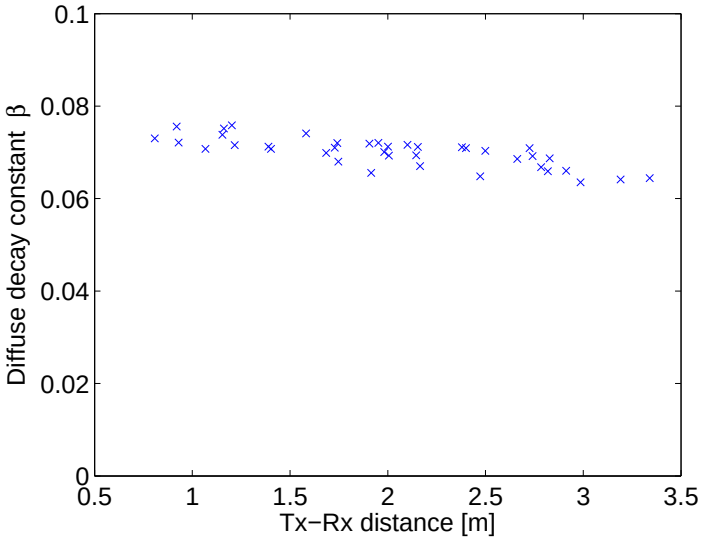

Figure 4.9: Diffuse decay constant against Tx-Rx distance in the angiography room.

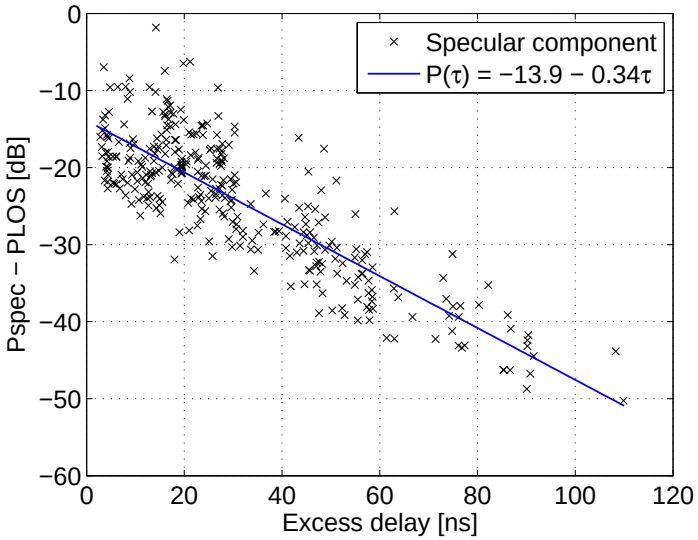

Figure 4.10: Dependency of the peak power of specular components normalized to the LOS component with respect to the excess delay. Results are from all the measurements in the angiography room.

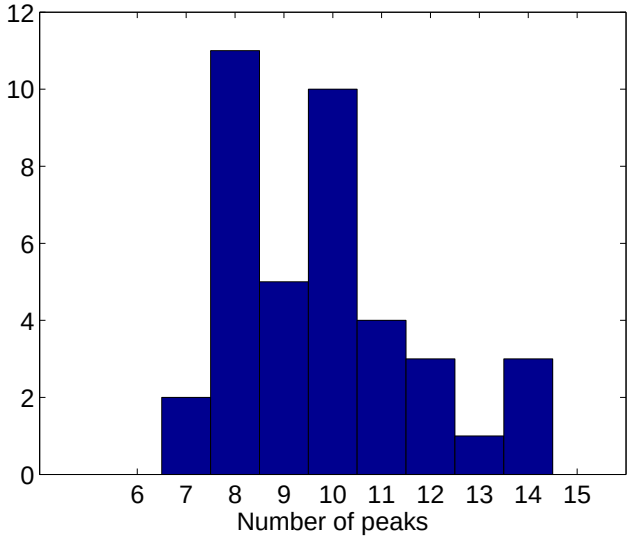

Figure 4.11: Distribution of the number of peaks in the angiography room.

Shielded room A total of 64 PDP's were modeled by the method presented in Chapter 4.3.4. The number of clusters varied between 1 and 5. Table 4.2 summarizes the number of PDP's which were modeled with 1 to 5 clusters, showing that most of PDP's were modeled by 3 clusters. Statistical modeling of cluster parameters in Eqs.(4.12) and (4.13) was based only on PDP's fitted with 3 clusters, considering the largest number of realizations.

Table 4.2: Number of PDP realizations modeled by a particular number of clusters.

# of clusters	1	2	3	4	5
# of PDP's	8	2	43	10	1

The analysis shows a strong correlation between decay constant α_n and peak power P_{n0}, thereby a possibility to simplify the degree of freedom in model parameters emerges. Cumulative distribution functions (CDF's) of each cluster parameter were found to follow the Gaussian distribution. The model parameters of the Gaussian distribution, *i.e.*, mean, μ, and standard deviation, σ, are listed in Table 4.3. It is worth noting that the model parameter for the peak power includes a large-scale effect, *i.e.*, path loss.

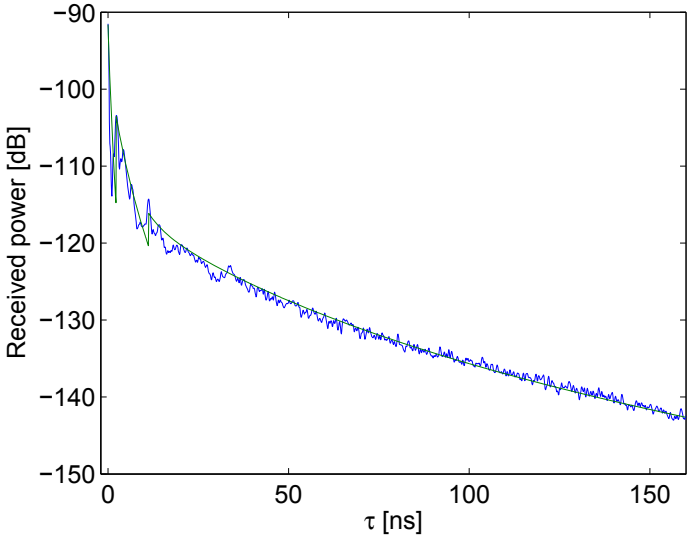

Figure 4.12: An example of measured PDP from the shielded room and its fitting using the power law model. Three clusters were identified in this PDP.

The CDF of the offset delay, τ_0, was found to fit well with the gamma distribution, as seen in Fig. 4.13. The Gamma distribution is determined by a shape parameter, k, and scale parameter, θ. Moderate correlation of 0.7 was observed between the second and third clusters, *i.e.,* between τ_{20} and τ_{30}. The best-fit model parameters of the Gamma distribution are listed in Table 4.3.

The peak delay, λ_n, represents the excess delay time where a new cluster starts. In modeling the peak delay, it was found that different distributions fit best for the second and third clusters. It is not necessary to model the peak delay of the first cluster, λ_1, since it always starts at $\tau = 0$. Figure 4.14 shows a CDF of λ_2 and λ_3, revealing that λ_2 follows the Gaussian distribution with the mean 2.2 and the standard deviation 0.37, whereas λ_3 was best modeled with the exponential distribution with the mean 9.1. It was also found that λ_2 had much smaller range of values than λ_3. This is probably because the second cluster is originated from a scatterer located close to the antennas such as a table, while the third cluster is attributed to far scatteres, for example, metal walls and ceiling.

Table 4.3: List of model parameters for peak power, decay factor, and offset delay.

Cluster	P_{n0}: Gaussian		α_n: Gaussian		Correlation	τ_{n0}: Gamma	
#	μ	σ	μ	σ	$\rho_{P_{n0}\alpha_n}$	k	θ
1	−60.9	6.1	7.9	1.1	0.8	26.6	0.08
2	−30.3	15.9	7.4	1.9	0.8	1.7	4.5
3	−31.9	12.0	4.7	0.5	1.0	6.9	7.1

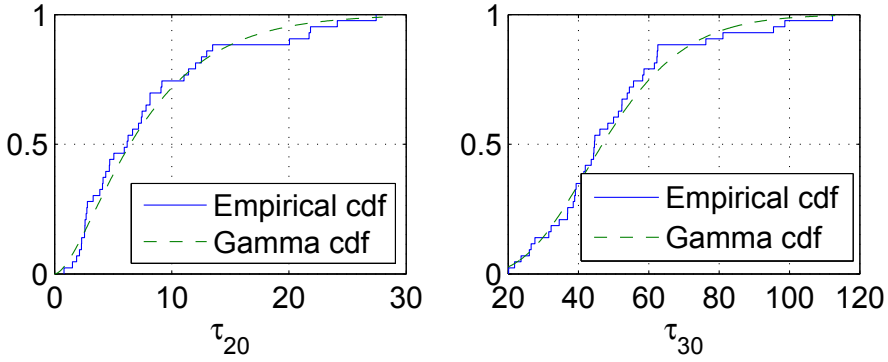

(a) (b)

Figure 4.13: The cumulative distribution functions of parameters τ_{20} (a) and τ_{30} (b), with best fit gamma distributions.

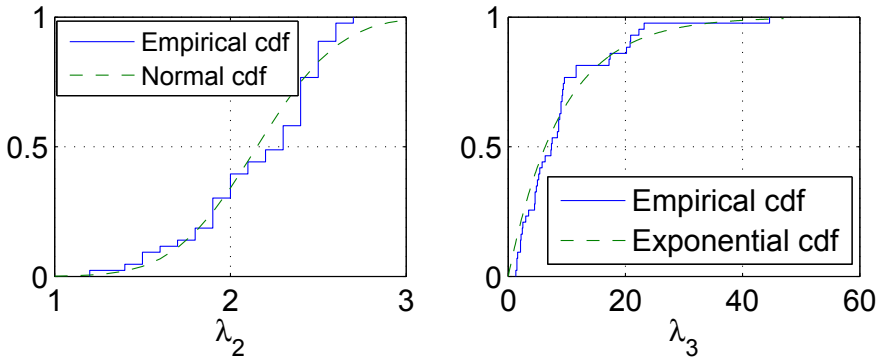

(a) (b)

Figure 4.14: CDFs of (a) λ_2 fitted with a Gaussian distribution and (b) λ_3 fitted with an exponential distribution.

5 Conclusions

In this work, path loss and delay domain analysis were made based on data from 60 GHz propagation channel measurements performed in hospital environments. Obtained power delay profiles were used to develop delay domain channel models for both environments. Additionally, preliminary measurements were performed in a shielded room, and the results were used to compare with actual hospital environments.

Antenna radiation patterns were measured in an anechoic chamber to get more accurate path loss results with radiation pattern compensation. It was possible to save time and effort without impairing the accuracy of the results by measuring only elevation patterns, because at 60 GHz most of the power is transmitted vie the line-of-sight path.

Removing the antenna gain from the path loss was useful, because then measurement data from different scenarios with different antenna combinations could be used to get a more general path loss model. Based on measurements performed in a shielded room, it was originally assumed that the hospital environments with shielded walls could have exceptional path loss values. However, it was found that the path loss in both hospital rooms was very similar to common indoor environments.

The delay domain characteristics of the two different hospital rooms were found to be very different from each other. The multipath components were very strong in the angiography room, which is probably at least partially caused by reflections from the large X-ray device near the antennas. In the ultrasonic imaging room there were less such large objects. The delay domain properties in the shielded room with metal walls were also found to be similar to the ultrasonic inspection room with concrete walls, meaning that nearby objects have a greater effect on the delay domain properties than far scatterers.

For future work the model parameter for the ultrasonic imaging room need to be derived and the statistical properties of both models have to be examined. With the statistical properties, the channel models can be implemented and tested against actual measurement data to verify them.

References

[1] S. R. Saunders and A. Aragón-Zavala, *Antennas and Propagation for Wireless Communication Systems.* 2nd Edition. John Wiley & Sons, Chichester, UK, 2007.

[2] T. S. Rappaport, *Wireless Communications: Principles and Practice.* 2nd Edition. Prentice Hall, NJ, USA, 2002.

[3] K. Yee, "Numerical solution of initial boundary value problems involving Maxwell's equations in isotropic media," *IEEE Transactions on Antennas and Propagation,* vol. 14, no. 3, pp. 302-307, 1966.

[4] R. Harrington, *Field Computation by Moment Methods.* Wiley-IEEE Press, NJ, USA, 1993.

[5] T. Fugen, J. Maurer, T. Kayser, and W Wiesbeck, "Capability of 3-D ray tracing for defining parameter sets for the specification of future mobile communications systems," *IEEE Transactions on Antennas and Propagation,* vol. 54, no. 11, pp. 3125-3137, 2006.

[6] J. Poutanen, K. Haneda, J. Salmi, V.-M. Kolmonen, A. Richter, P. Almers, and P. Vainikainen, "Development of measurement-based ray tracer for multi-link double directional propagation parameters," *Proc. 3rd European Conference on Antennas and Propagation (EuCAP 2009),* Berlin, Germany, March 23-27, 2009, pp. 2622-2626

[7] A. A. M Saleh and R. A. Valenzuela, "A statistical model for indoor multipath propagation," *IEEE Journal on Selected Areas in Communications*, vol. 5, pp. 128-137, February 1987.

[8] P. F. M. Smulders and L. M. Correia, "Characterisation of propagation in 60 GHz radio channels," *Electronics and Communication Engineering Journal,* vol. 9, no. 2, pp. 73-80, April 1997.

[9] T. Zwick, T. J. Beukema, and H. Nam, "Wideband channel sounder with measurements and model for the 60 GHz indoor radio channel," *IEEE Transactions on Vehicular Technology*, vol. 54, no. 4, pp. 1266-1277, July 2005.

[10] N. Moraitis and P. Constantinou, "Measurements and characterization of wideband indoor radio channel at 60 GHz," *IEEE Transactions on Wireless Communications*, vol. 5, no. 4, pp. 880-889, April 2006.

[11] J. Kivinen, "60-GHz wideband radio channel sounder," *IEEE Transactions on Instrumentation and Measurement,* vol. 56, no. 5, pp. 1831-1838, October 2007

[12] S. Ranvier, M. Kyrö, K. Haneda, T. Mustonen, C. Icheln, and P. Vainikainen, "VNA-based wideband 60 GHz MIMO channel sounder with 3-D arrays", *Proc. IEEE RWS 2009 Radio and Wireless Symposium*, San Diego, CA, 18-22 January 2009, CD-ROM (ISBN 978-1-4244-2699-7), pp. 308-311.

[13] S.-K. Yong,"TG3c channel modeling sub-committee final report," *IEEE802.15-07-0584-01-003c*, March 2007.

[14] P. Nobles, and F. Halsall, "Indoor propagation at 17 GHz and 60 GHz-measurements and modelling," *IEE National Conference on Antennas and Propagation*, York, UK, 31 March-1 April, 1999, pp. 93 - 96.

[15] M. Kyrö, J. Simola, K. Haneda, S. Ranvier, P. Vainikainen, and K. Takizawa, "60GHz radio channel measurements and modeling in a shielded room," *IEEE VTC 2010-Spring 71st Vehicular Technology Conference*, Taipei, Taiwan, 16-19 May 2010, paper: session 3H, 5.

[16] H. Harada *et al.*, "Channel model Matlab code release" *IEEE 802.15.07-0648-00-003c*, Orlando, USA, March 2007.

[17] P. Pagani, I. Siaud, N. Malhouroux, and W. Li, "Adaptation of the France Telecom 60 GHz channel model to the TG3c framework," *IEEE 802.15-06-0218-00-003c*, April 2006.

[18] D. Cassioli, M. Z. Win, and A. F. Molisch, "The Ultra-Wide Bandwidth Indoor Channel: From Statistical Model to Simulations," *IEEE Journal on Selected Areas in Communications*, vol. 20, No. 6. August 2002, pp 1247-1257.

[19] J. Karedal, S. Wyne, P. Almers, F. Tufvesson, and A. F. Molisch, "Measurement-based statistical model for industrial ultra-wideband channels," *IEEE Transactions on Wireless Communications,* vol. 6, no. 8, pp. 3028-3037, August 2007.

[20] J. B. Andersen and P. Eggers, "A heuristic model of power delay profiles in landmobile Communications," *Proc. 1992 URSI International Symposium on Electromagnetic Theory*, Sydney, Australia, August 17-20, 1992, pp. 55-57.